Supporting Information for

Anode/cathode Dual-purpose Aluminum Current Collectors for Aqueous Zinc-ion Batteries

Ruijie Zhu†, Zetao Xiong†, Huijun Yang, Ning Wang, Sho Kitano, Chunyu Zhu*, Yoshitaka Aoki, and Hiroki Habazaki.*

Ruijie Zhu - Graduate School of Chemical Sciences and Engineering, Hokkaido University, Sapporo, Hokkaido 060-8628, Japan

Zetao Xiong - Graduate School of Chemical Sciences and Engineering, Hokkaido University, Sapporo, Hokkaido 060-8628, Japan

Huijun Yang - National Institute of Advanced Industrial Science and Technology (AIST), 1-1-1, Umezono, Tsukuba 305-8568 Japan.

Ning Wang - Huangpu Hydrogen Energy Innovation Centre, School of Chemistry and Chemical Engineering, Guangzhou University, Guangzhou 510006, China

Sho Kitano - Division of Applied Chemistry, Faculty of Engineering, Hokkaido University, Sapporo, Hokkaido 060-8628, Japan

Chunyu Zhu - School of Low-carbon Energy and Power Engineering, China University

of Mining and Technology, Xuzhou 221116, China

Yoshitaka Aoki - Division of Applied Chemistry, Faculty of Engineering, Hokkaido University, Sapporo, Hokkaido 060-8628, Japan

Hiroki Habazaki - Division of Applied Chemistry, Faculty of Engineering, Hokkaido University, Sapporo, Hokkaido 060-8628, Japan

Corresponding Author

* Chunyu Zhu - School of Low-carbon Energy and Power Engineering, China University of Mining and Technology, Xuzhou 221116, China

* Huijun Yang - National Institute of Advanced Industrial Science and Technology (AIST), 1-1-1, Umezono, Tsukuba 305-8568 Japan.

E-mail: zcyls@cumt.edu.cn

yang.hj@aist.go.jp

Supplemental Experiments

Preparation of the active materials: The preparation of α-MnO_2 and VO_2 nanowires were referred by previous reports. [Ref 1,2] For the MnO_2, first, 2.845g $MnSO_4$ and 7.112g $KMnO_4$ were dissolved in 150 mL DI water. After stirring, the solution was transferred to a hydrothermal autoclave reactor. The α-MnO_2 nanowires can be obtained after 12 h hydrothermal reaction at 140 ℃. For the VO_2, firstly, 0.25 g V_2O_5 was dispersed into graphene oxide dispersion (2 mg mL^{-1}). After stirring, the suspension was transferred to a hydrothermal autoclave reactor, and the reaction was proceeded at 180 °C for 12 h to form a gel-like precursor. The VO_2 could be obtained after the gel was reduced by ascorbic acid (Vitamin C, VC) under 80°C in a water bath.

Preparation of the cathodes: For the full cell tests, different active materials (MnO_2, VO_2 or AC) were mixed with Ketjen Black (KB), Polytetrafluoroethylene (PTFE) in ethanol to form a slurry. The cathodes were prepared by the blade-casting method, in which, the slurry with different active materials (MnO_2, VO_2 or AC) was coated onto the Al foils or the Al-Nb foils to prepare the current collector@active material cathode. The Ti mesh supported cathodes were prepared by pressing the slurry onto the Ti mesh (Nilaco, Japan, 100 mesh). All the foils and meshes were cut into disk electrodes (10 mm in diameter) for Swagelok cells, or rectangle (5 cm × 7 cm) for pouch cells.

Electrochemical measurements*:* The electrochemical impedance spectra (EIS), linear sweep voltammetry (LSV), cyclic voltammetry (CV) measurements were all tested on an electrochemical

workstation (Princeton VersaSTAT3). For the EIS measurement, the frequency range was 100 kHz to 0.1 Hz. For the LSV tests, the sweep rate was 5 mV s^{-1}. For the CV tests, the sweep rate was 0.5 mV s^{-1}.

Calculation details: We have employed the plane-wave code Vienna ab-initio simulation package (VASP) program [Ref 3,4] to perform all the spin-polarized density functional theory (DFT) calculations within the generalized gradient approximation (GGA) using the Perdew-Burke-Ernzerhof (PBE) [Ref 5] formulation. We have chosen the projected augmented wave (PAW) potentials [Ref 6,7] to describe the ionic cores and take valence electrons into account using a plane wave basis set with a kinetic energy cutoff of 500eV. The valence electron configurations applied in this work are $3s^2 3p^1$(Al), $5s^1 4d^4$(Nb), $4s^2 3d^2$(Ti), $4s^1 3d^{10}$(Cu), $2s^2 2p^4$ (O), and $1s^1$(H), respectively. Partial occupancies of the Kohn−Sham orbitals were allowed using the Gaussian smearing method and a width of 0.02 eV. The electronic energy was considered self-consistent when the energy change was smaller than 10^{-6} eV.

The G values are calculated by:

$G = H - T\Delta S = E_{DFT} + E_{ZPE} - TS$

E_{DFT} is the total energy from the DFT calculation. E_{ZPE} is the zero-point energy, S is the entropy and T is the temperature (298K).

The Cu (100) surface slab was constructed with 5 atomic layers, which contains 107 Cu atoms. The Nb (100) surface slab was constructed with 5 atomic layers, which contains

45 Nb atoms. The Al_2O_3 (001) surface slab was constructed with 8 atomic layers, which contains 36 Al and 48 O atoms. The TiO_2 (111) surface slab was constructed with 6 atomic layers, which contains 36 Ti and 56 O atoms. The Nb_2O_5 (001) surface slab was constructed with 6 atomic layers, which contains 42 Nb and 93 O atoms. This slab was separated by a 15 Å vacuum layer in the z direction between the slab and its periodic images. During structural optimizations of the (110) surface models, a 3×3×1 gamma-point centered k-point grid for Brillouin zone was used. And the atomic layers were allowed to fully relax.

Supplemental Figures

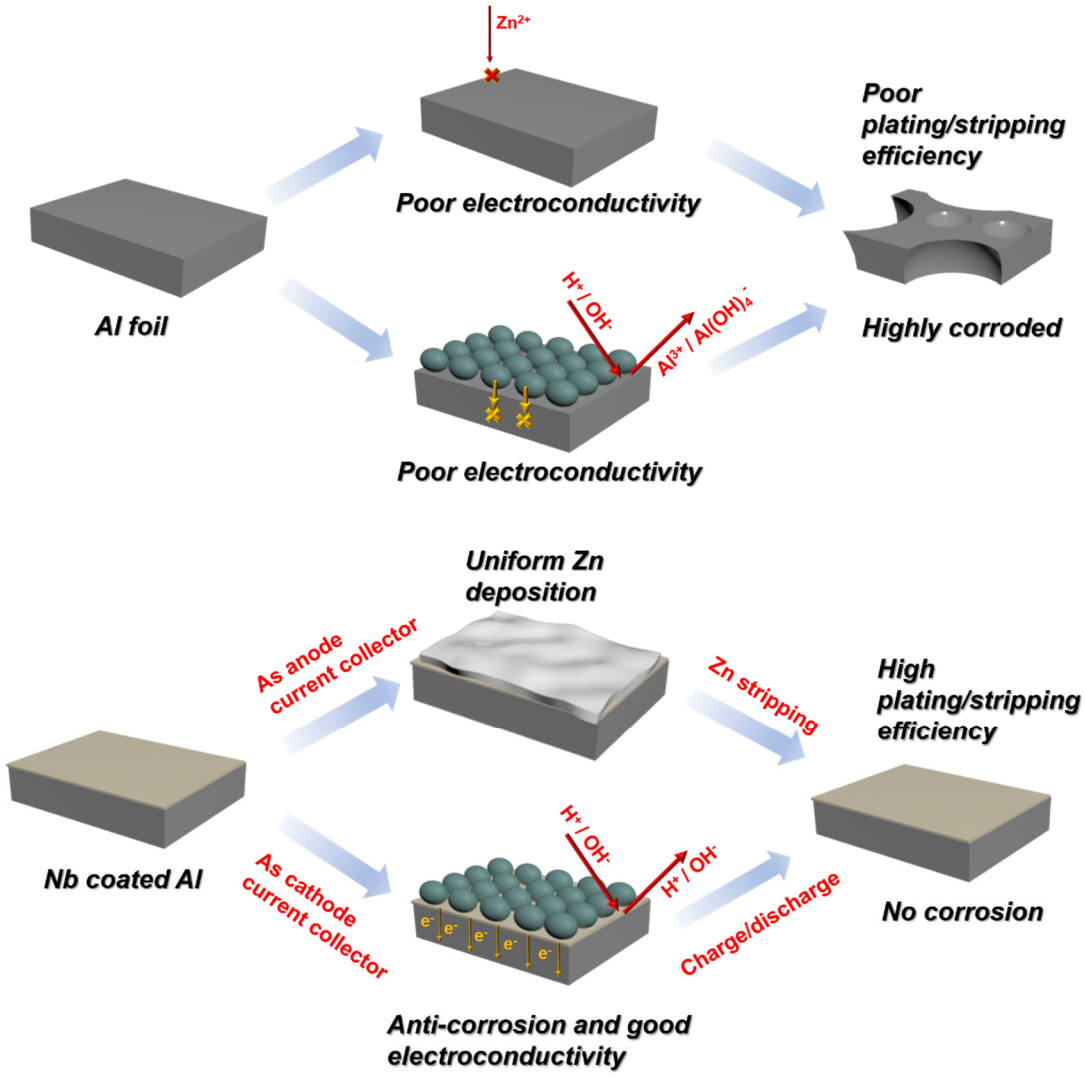

Figure S1. Schematic illustration of the difference between Al foil and Al-Nb when being used as anode/cathode current collectors for RAZIBs.

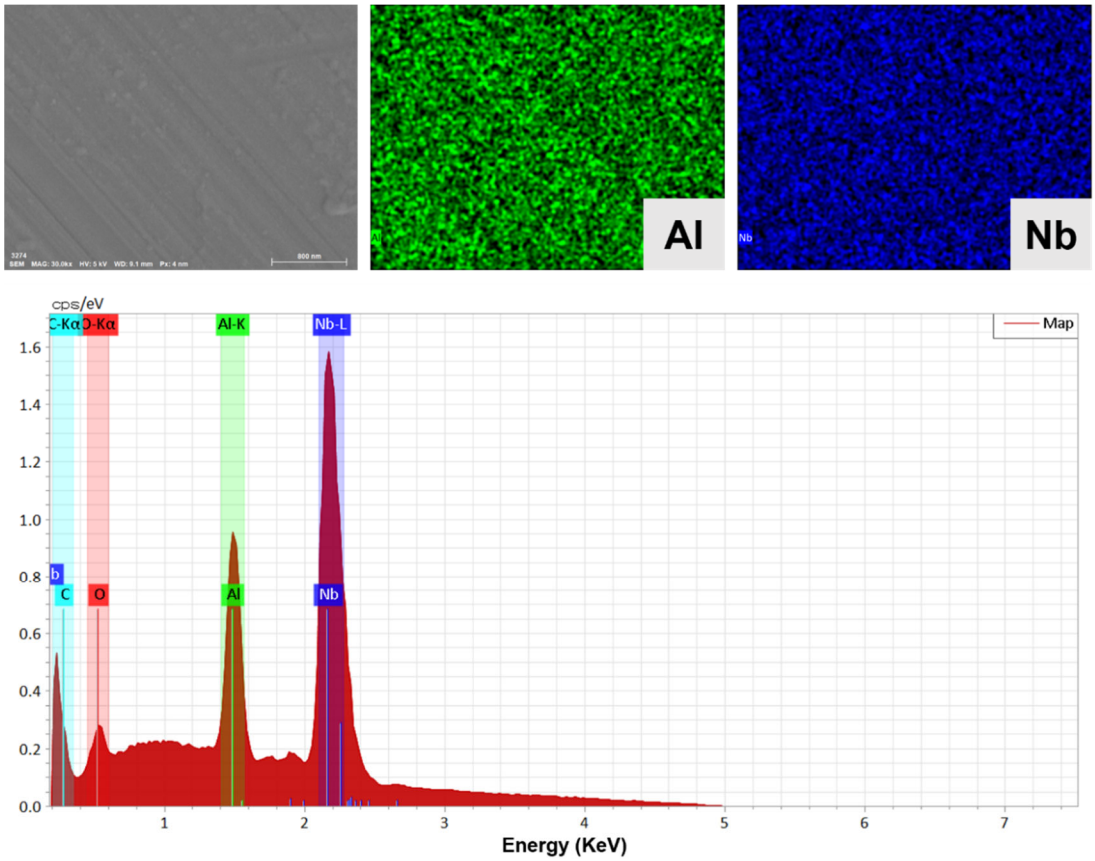

Figure S2. Top-view SEM image and the corresponding EDS mapping and spectra of the Al-Nb foils.

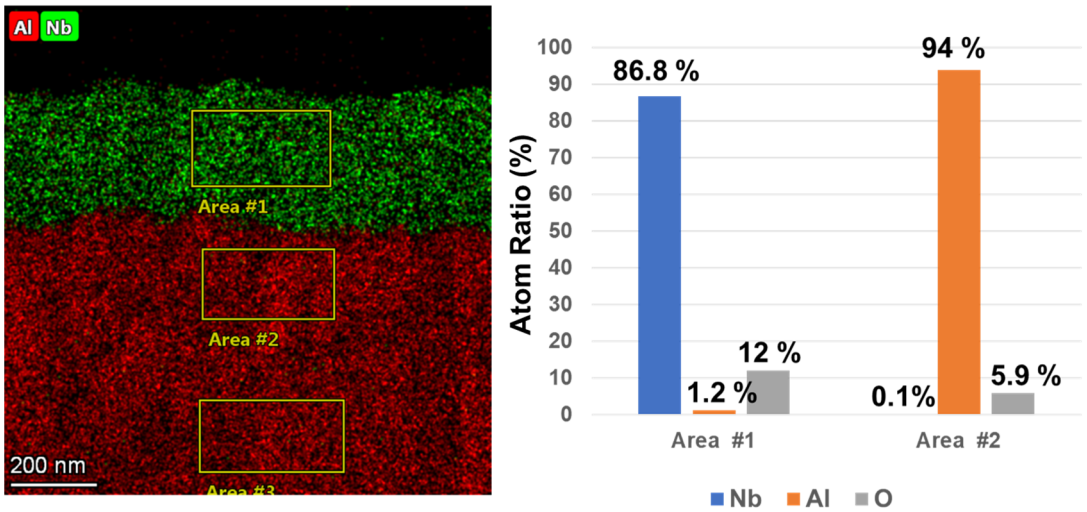

Figure S3. Atom ratios of different regions in STEM image of the Al-Nb sample.

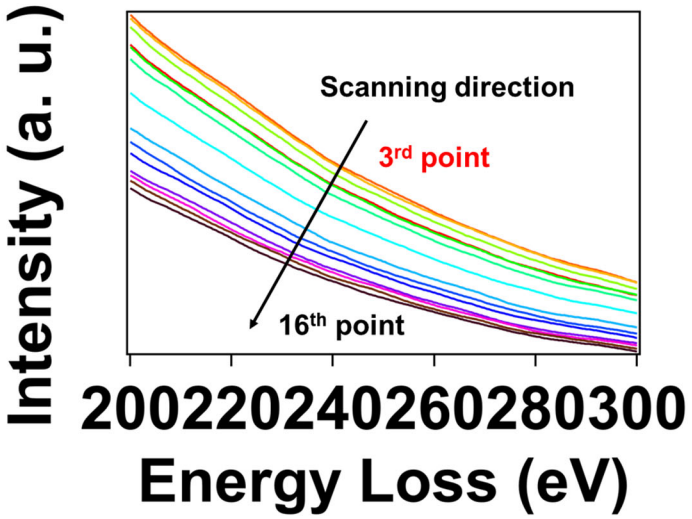

Figure S4. The EELS spectra of Nb taken from the outer surface (starting from the position A in Figure 1b_1). The peak of Nb_2O_5 no longer appears in the spectra.

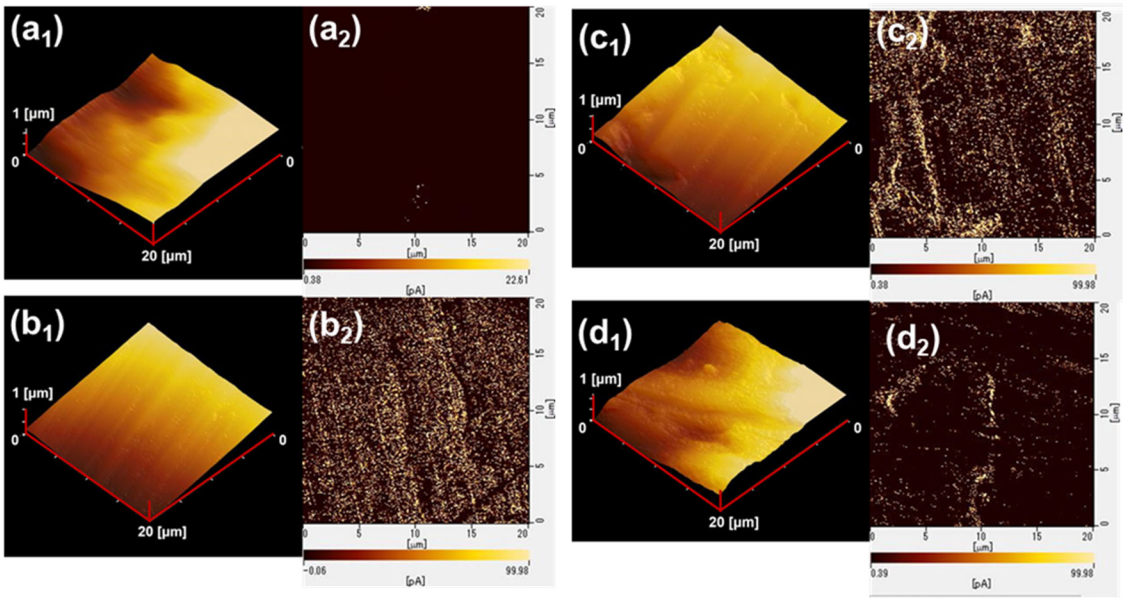

Figure S5. Conductive atomic force microscopy (c-AFM) observation of different metal substrates. a_1) 3D morphology and a_2) current map of the Al foil; b_1) 3D morphology and b_2) current map of the Al-Nb foil; c_1) 3D morphology and c_2) current map of the Cu foil;

d_1) 3D morphology and d_2) current map of the Ti foil.

Although both Al-Nb and Cu exhibit good surface conductivity, Zn may possess a more uniform nucleation behavior when deposited on the Al-Nb surface because the surface of the Cu sample is rougher than Al-Nb. Moreover, the tip effect can be also reduced due to the relatively smooth surface of Al-Nb.

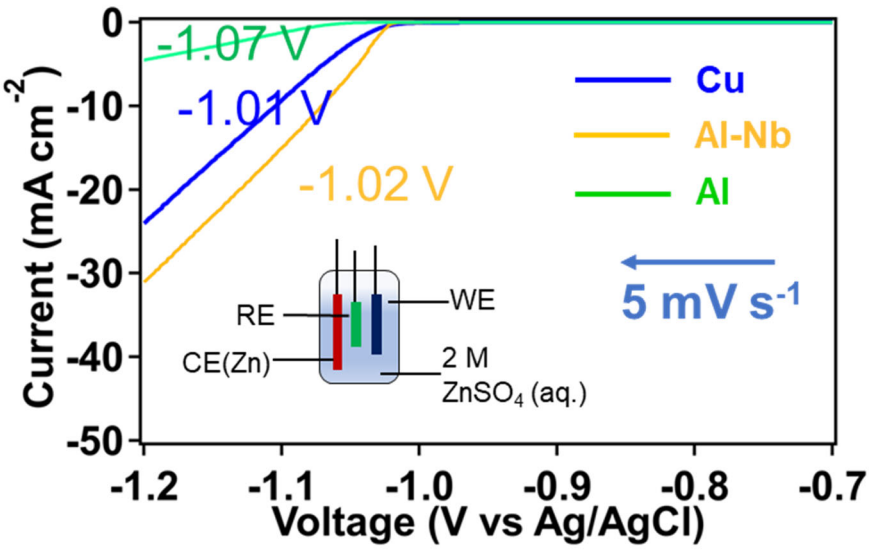

Figure S6. LSV curves of different substrates tested in the three-electrode cell. The electrolyte is 2 M $ZnSO_4$ aqueous solution. When the current density is -0.25 mA cm^{-2}, the potentials corresponding to the Cu foil, the Al-Nb foil and the Al foil are -1.01 V, -1.02 V, -1.07 V, respectively.

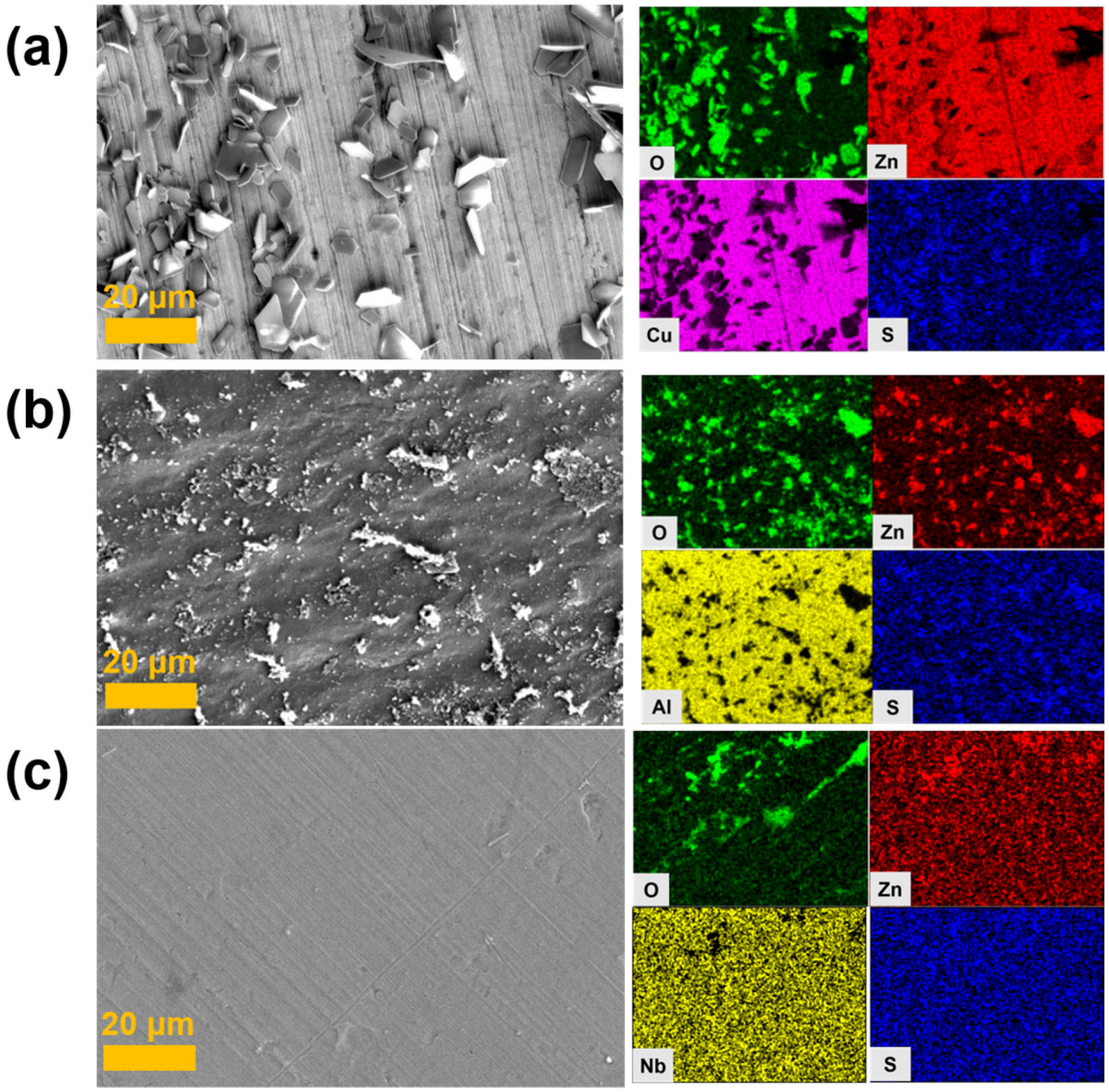

Figure S7. Top view of different metal substrates after the potentiostatic corrosion test. SEM images and the EDS mappings correspond to (a) the Cu foil, (b) the Al foil and (c) the Al-Nb foil after test.

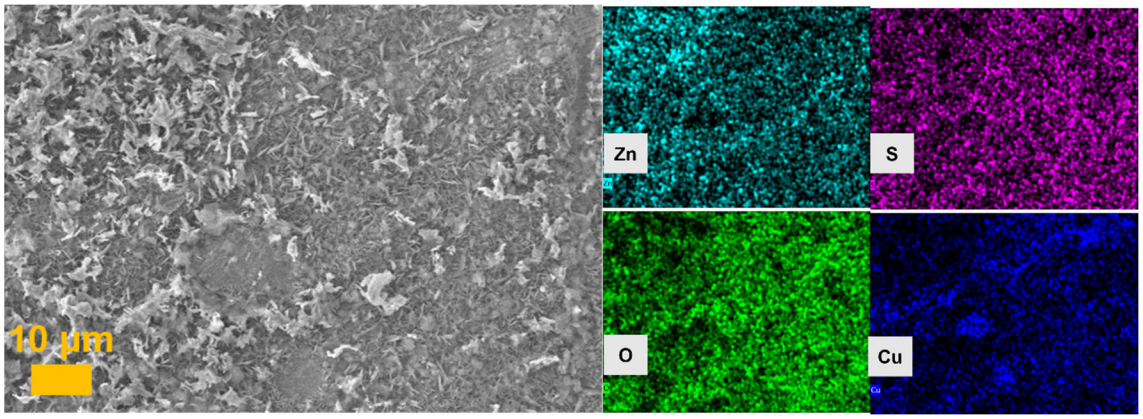

Figure S8. SEM image and EDS mappings of the Cu foil after Zn plating/stripping for one cycle.

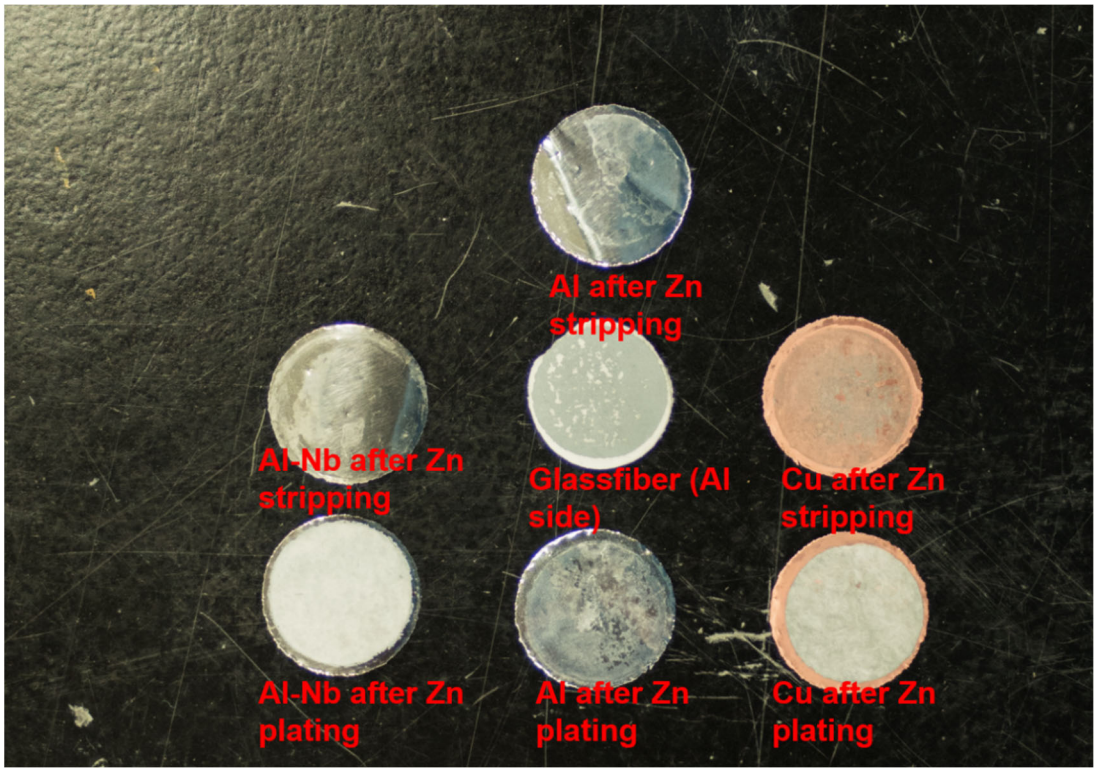

Figure S9. Optical photos of different metal substrates after Zn plating or Zn stripping.

Despite the high resistance of Al surface, Zn metal can still be electrodeposited onto the surface of Al under constant current. But there appears to be no adhesion between the

deposited Zn and the Al substrate. When we removed the separator, all the Zn metal was tightly bonded to the separator as we exhibited in the photo, and some corrosion traces can be seen on the surface of the Al.

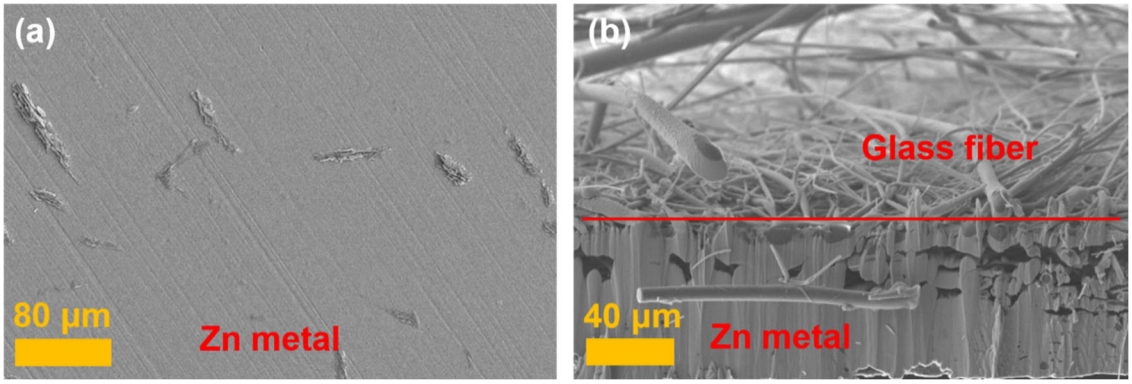

Figure S10. SEM images of Zn deposited on Al-Nb foil under high current density (25 mA cm^{-2}). (a) Top view of the Zn coating and (b) cross sectional observation of the Zn coating.

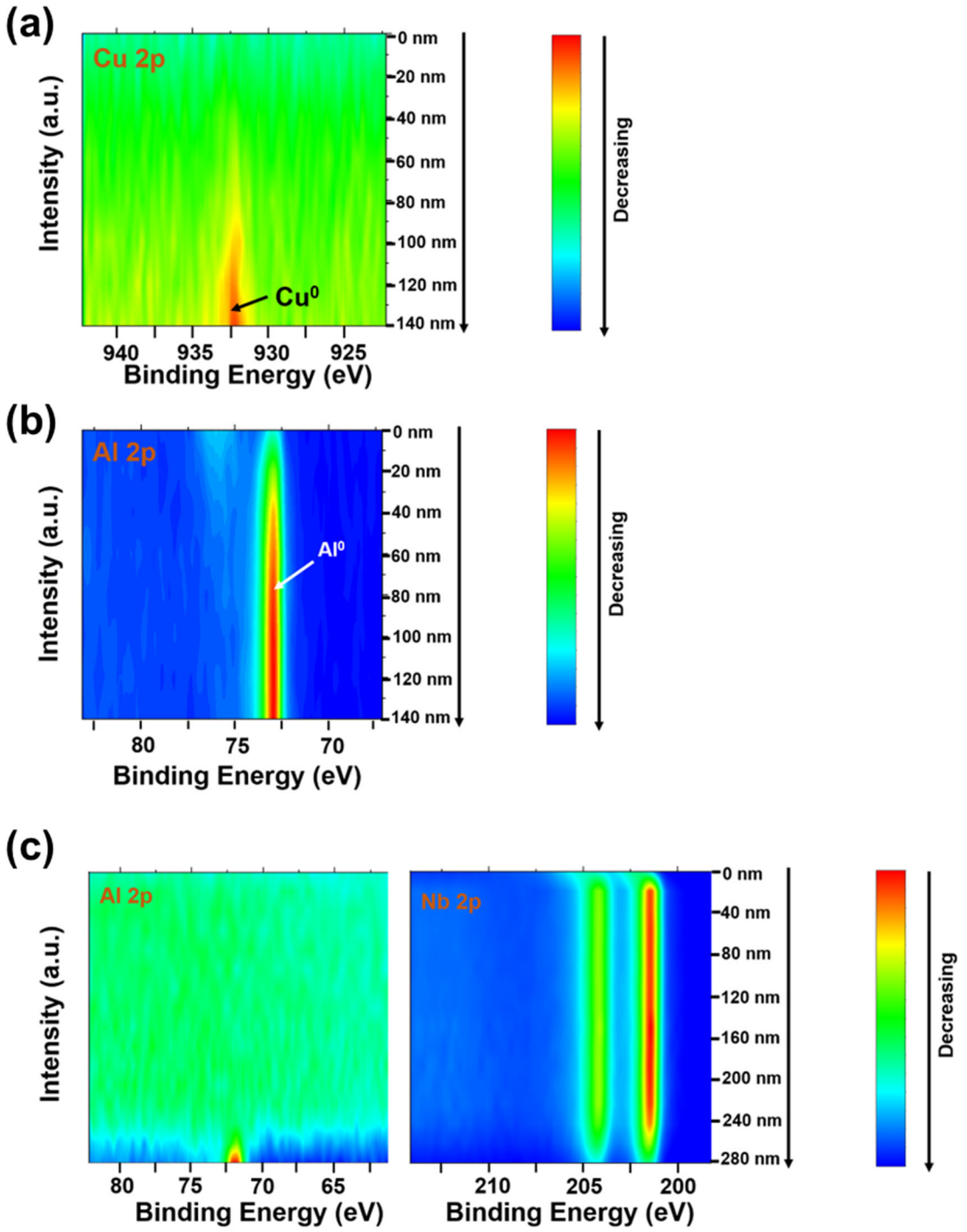

Figure S11. XPS depth profile of (a) the Cu foil, (b) the Al foil and (c) the Al-Nb foil after Zn stripping.

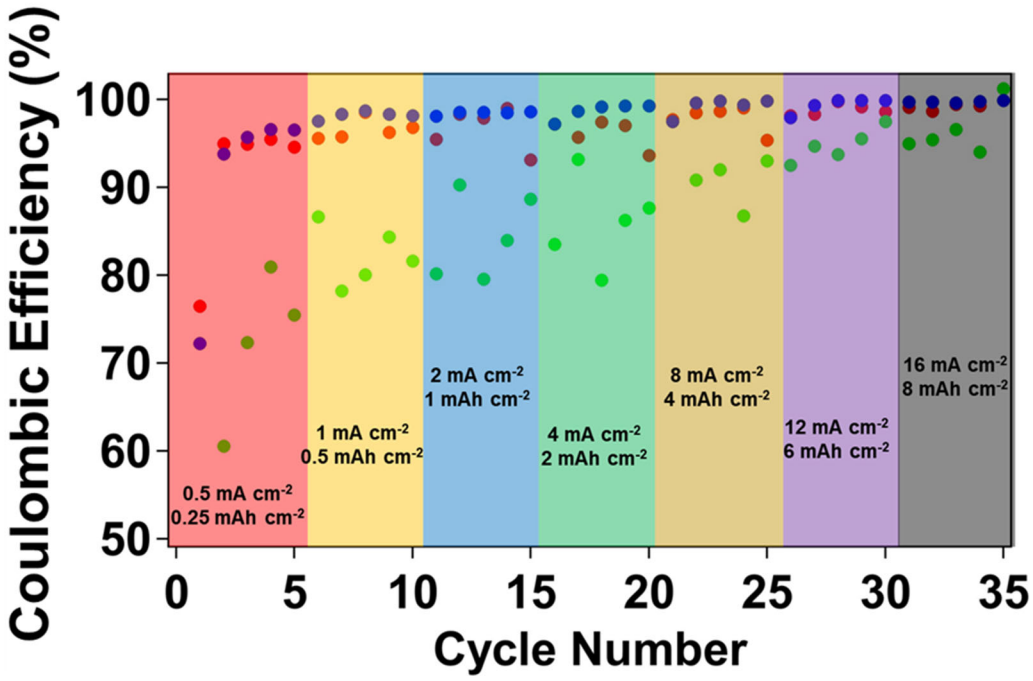

Figure S12. Zn plating/stripping rate performance of different substrates tested in the metal foil||Zn foil half-cells.

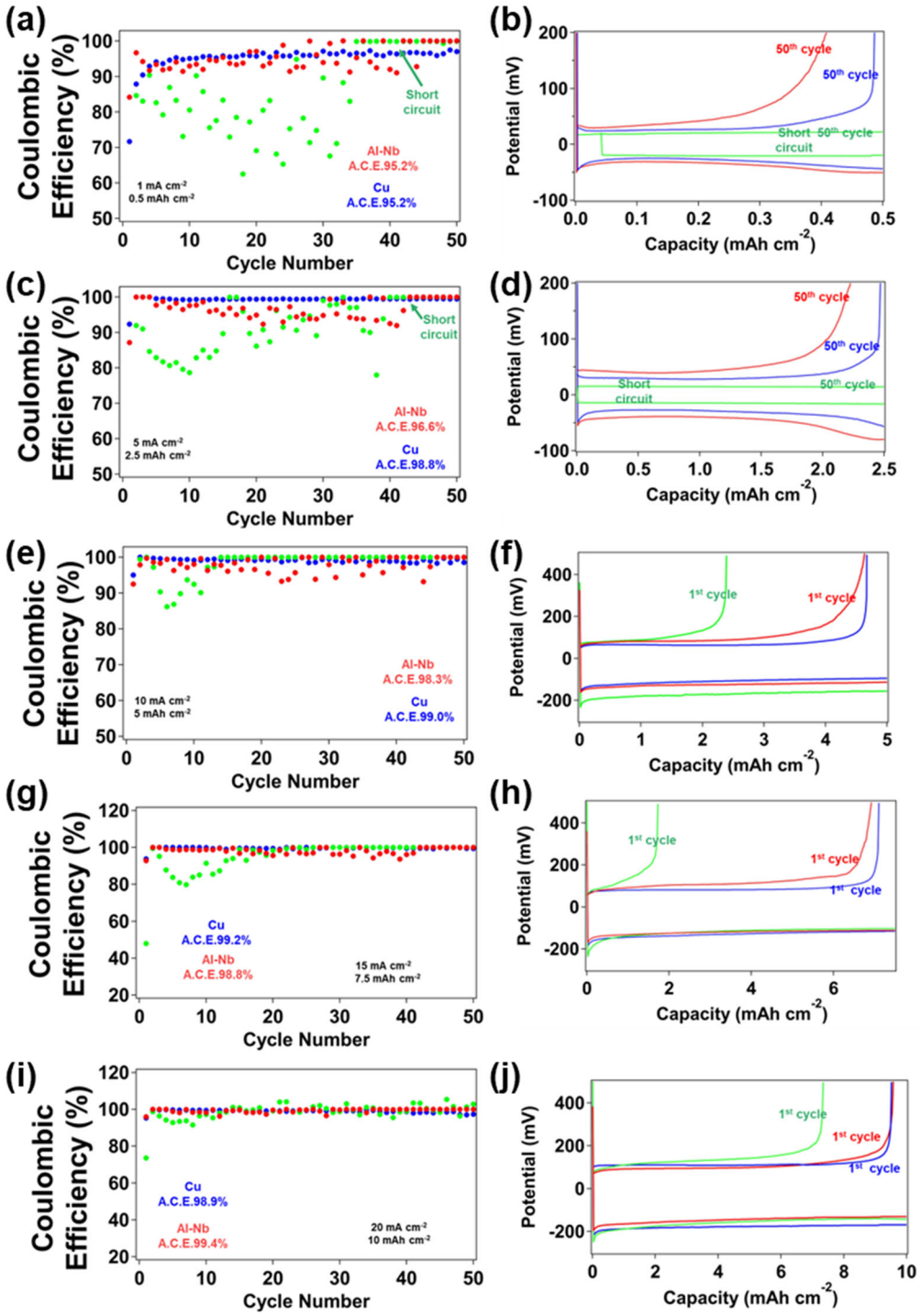

Figure S13. Coulombic efficiency of Zn plating/stripping when using different metal foils as the Zn deposition substrates. Coulombic efficiency of the cells tested under (a) 1 mA cm^{-2} (c) 5 mA cm^{-2} (e) 10 mA cm^{-2} (g) 15 mA cm^{-2} (i) 20 mA cm^{-2}. Corresponding voltage

profiles of (a) 1 mA cm^{-2} (c) 5 mA cm^{-2} (e) 10 mA cm^{-2} (g) 15 mA cm^{-2} (i) 20 mA cm^{-2}. The coulombic efficiency of Nb is slightly lower than that of Cu at low currents, because the nucleation of Zn at low currents can be blocked by the relatively high surface impedance. The overpotential at low currents cannot reach enough to induce uniform nucleation of Zn on the Nb surface due to the existed Nb_2O_5 passivation layer.

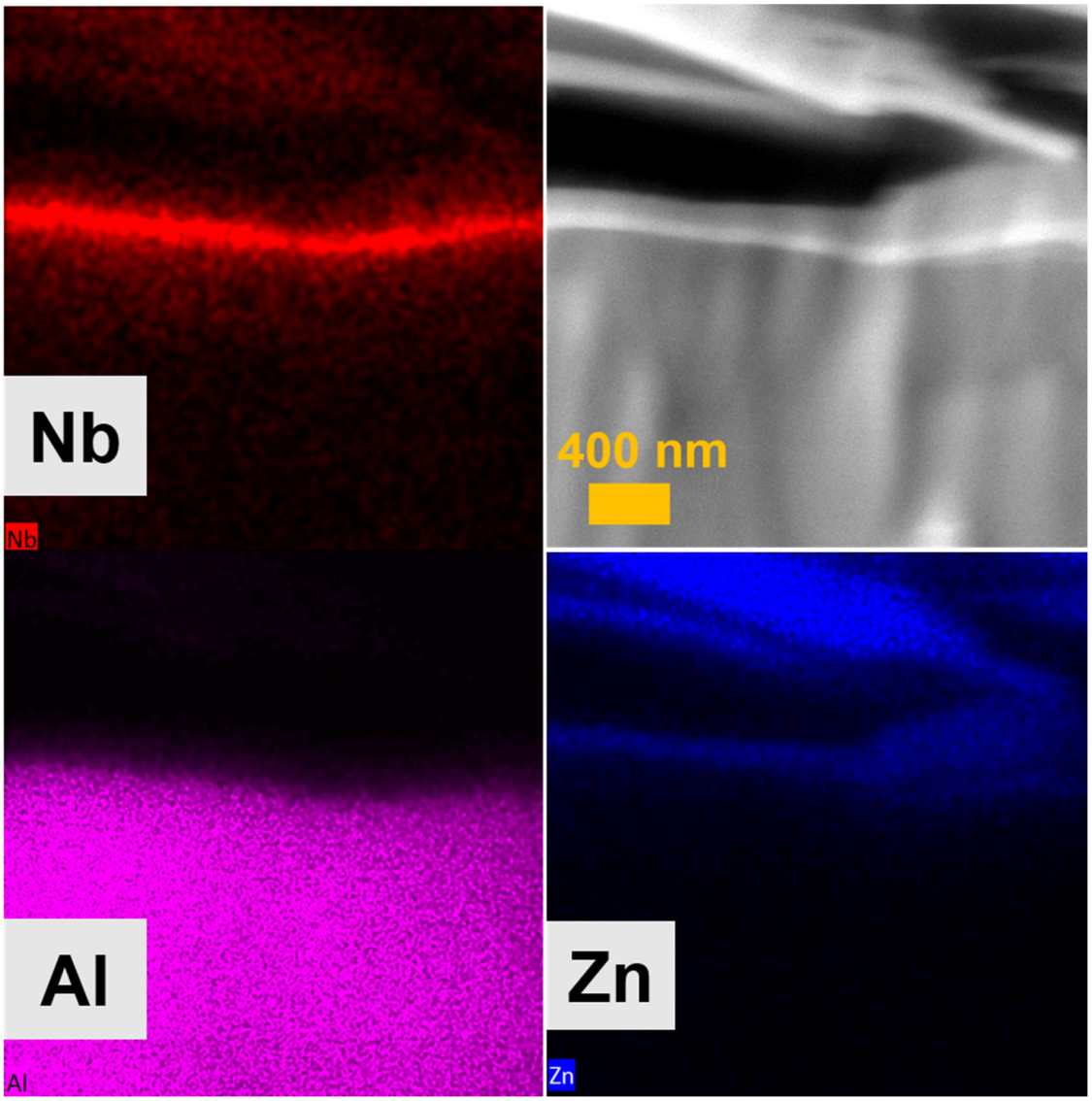

Figure S14. Cross-sectional SEM image and the corresponding EDS mappings of the Al-Nb foil after Zn deposition under low current density (0.1 mA cm^{-2}, 1 mAh cm^{-2}).

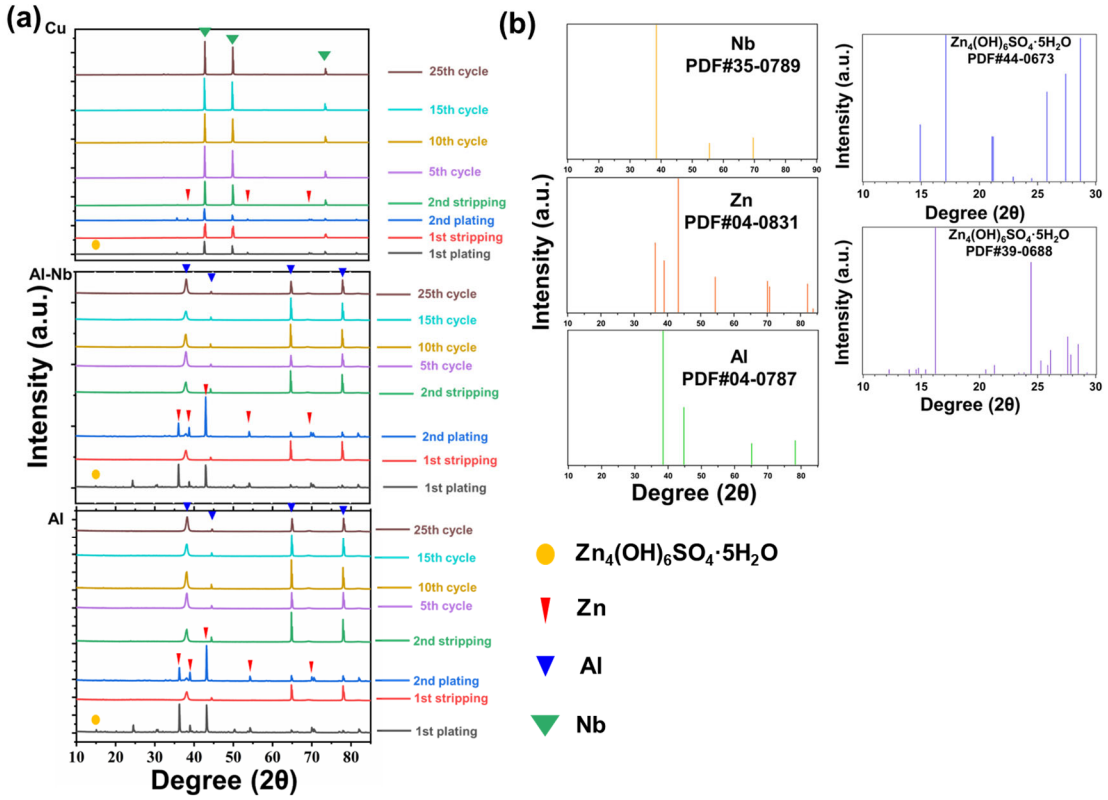

Figure S15. (a) Ex-situ XRD patterns of different substrates after Zn plating/stripping, from top to bottom are Cu, Al-Nb, and Al, respectively. (b) Standard XRD patterns of the related materials.

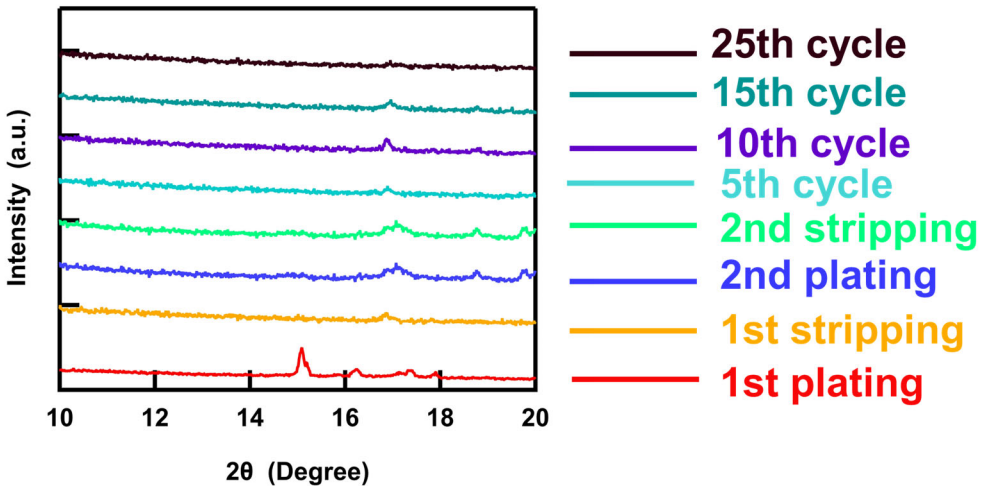

Figure S16. The enlarged XRD patterns of the Al foil corresponding to Figure S15

The peak appears at about 15.2 ° is considered belonging to $ZnSO_4 \cdot 6H_2O$ (PDF#32-1478).

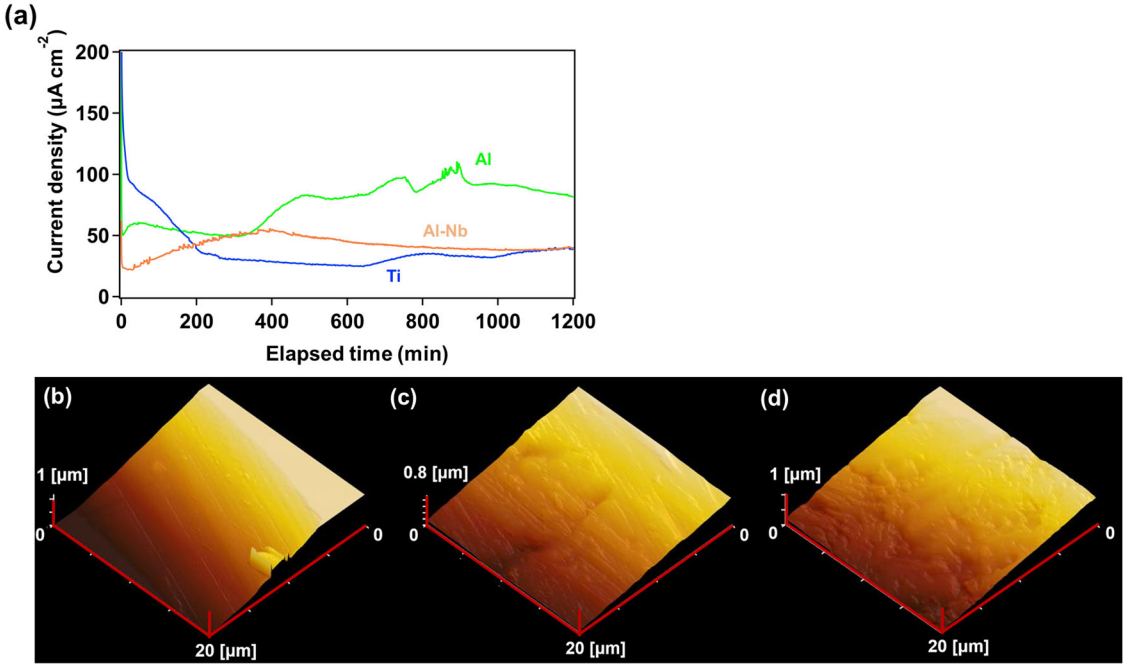

Figure S17. (a) Current profiles of different substrates under the 2 V (vs Zn) potentiostatic test. AFM images of the tested (b) Al foil (c) Al-Nb foil and (d) Ti foil, respectively.

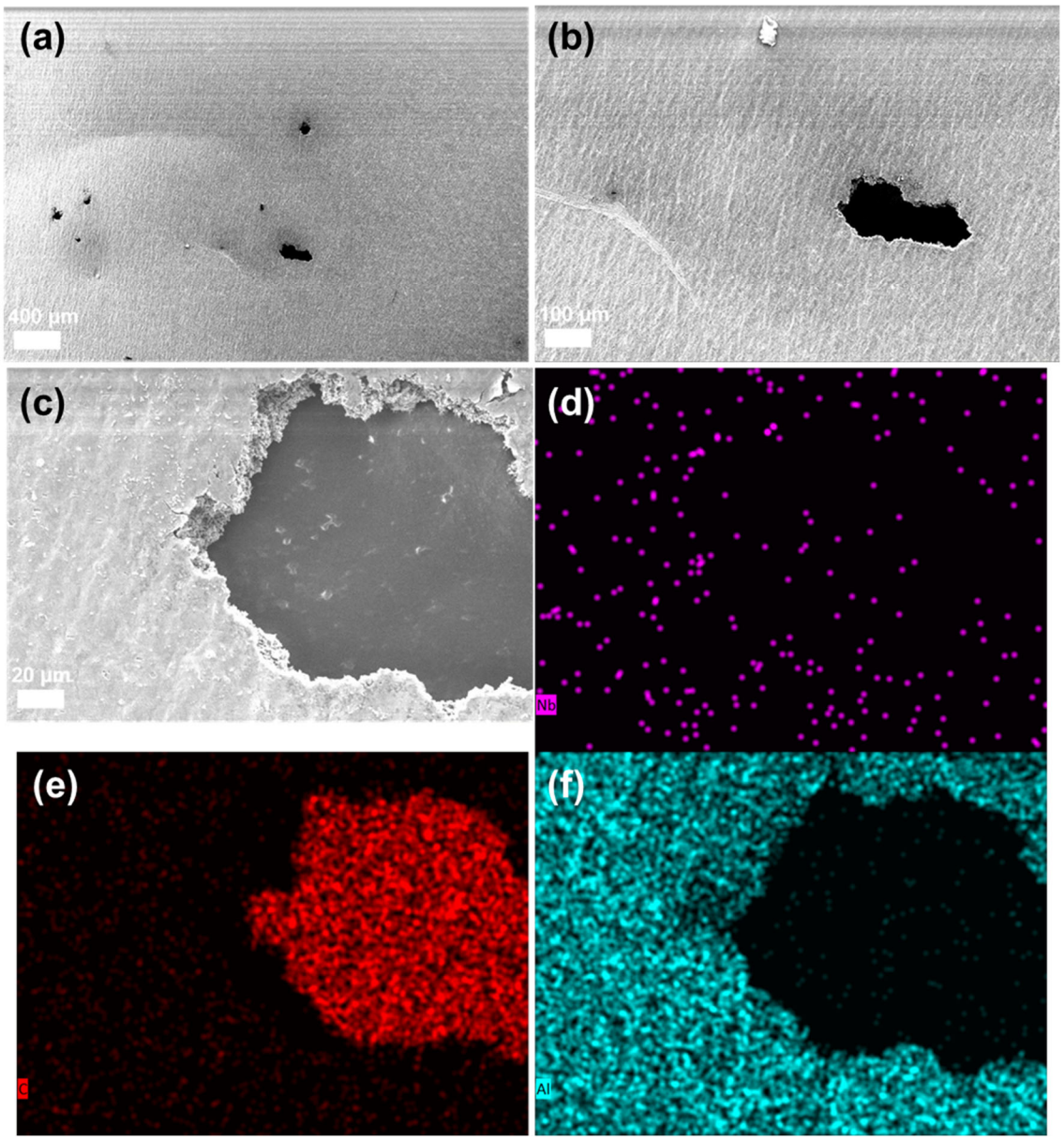

Figure S18. SEM images of (a, b, c) Al foil after the potentiostatic test, (d, e, f) elemental mappings of **Figure 18(c)**.

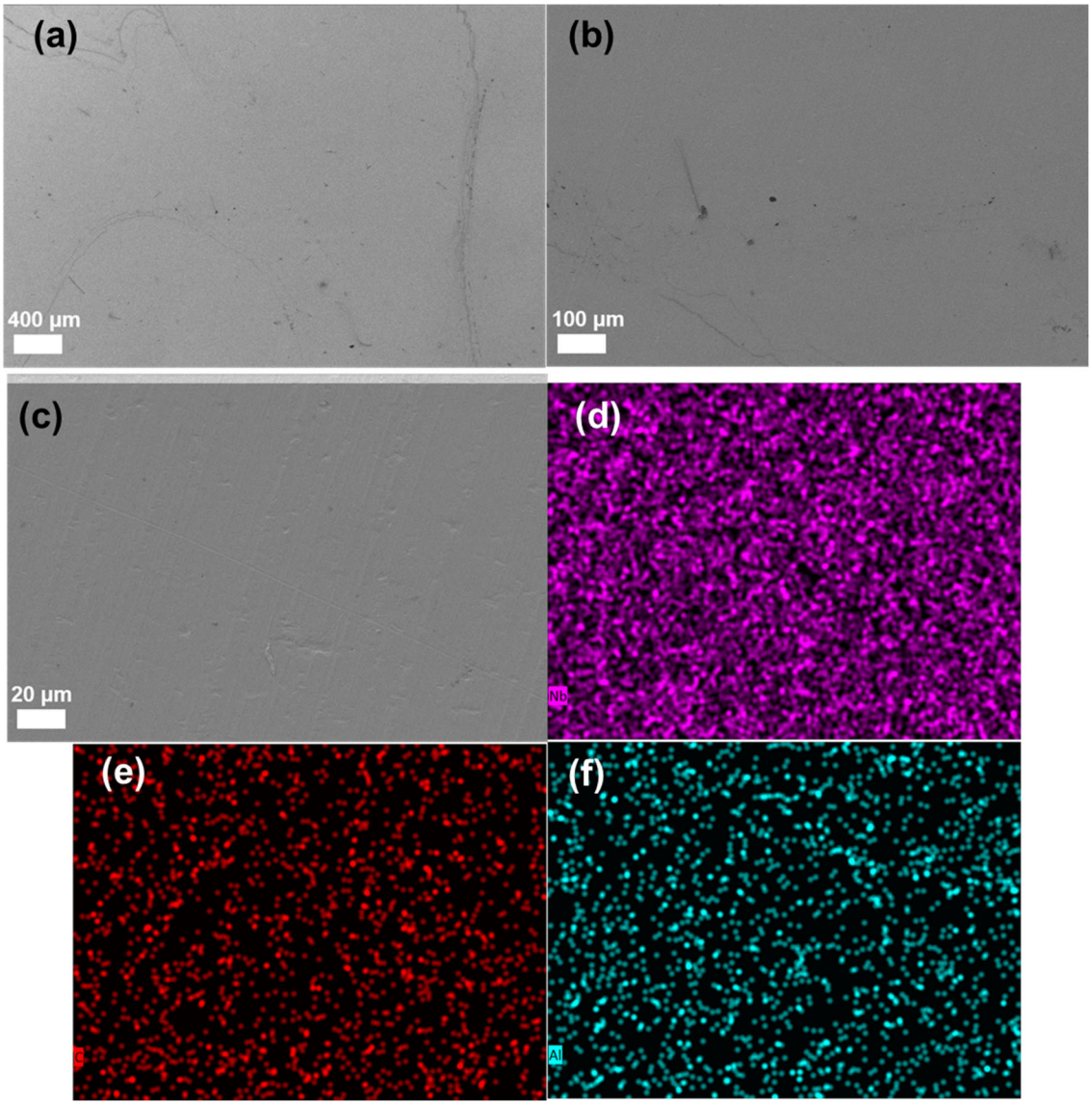

Figure S19. SEM images of (a, b, c) Al-Nb foil after the potentiostatic test, (d, e, f) elemental mappings of **Figure 19(c)**.

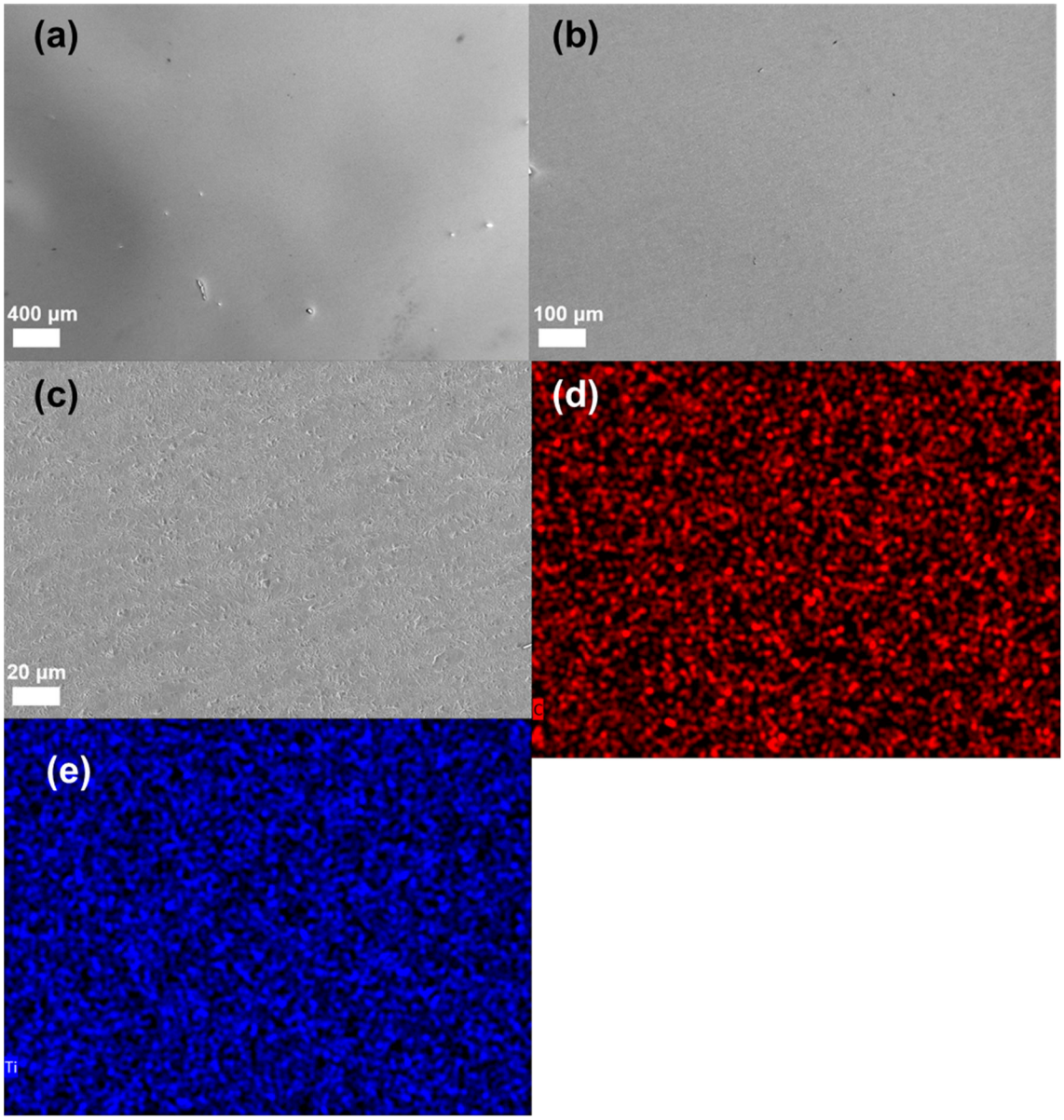

Figure S20. SEM images of (a, b, c) Ti foil after the potentiostatic test, (d, e) elemental mappings of **Figure 20(c)**.

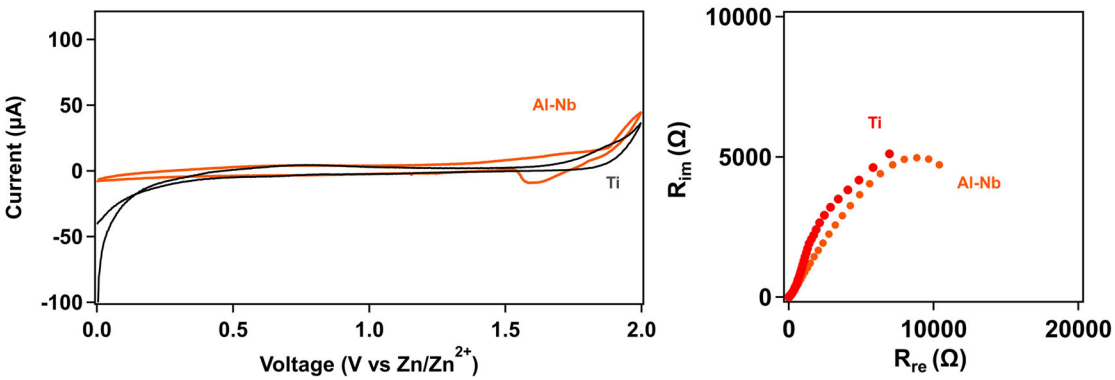

Figure S21. CV test of Zn||Ti foil half cells at the scanning rate of 0.5 mV s^{-1} (left), and the Nyquist plot of Zn||Ti foil half cells (right).

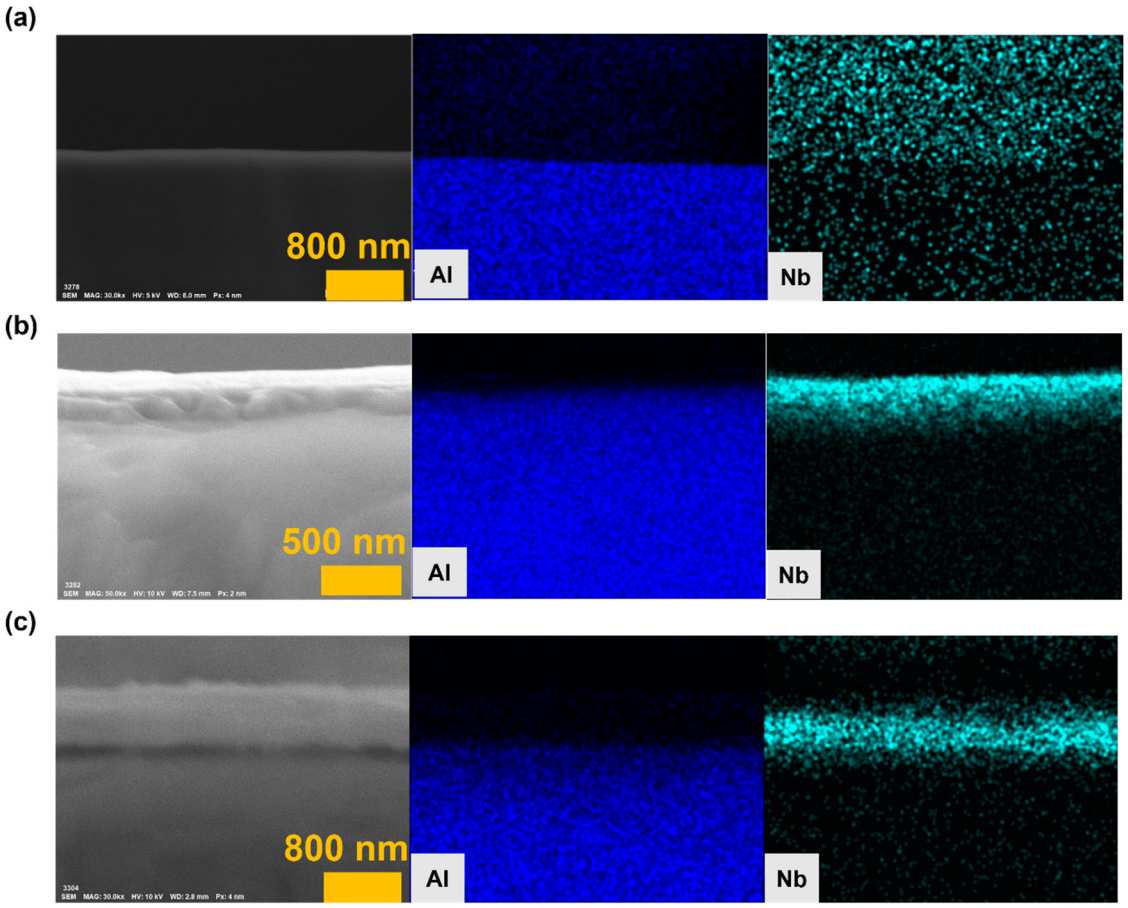

Figure S22. Cross sectional SEM images and the corresponding EDS mappings of the Al-Nb foils prepared by different sputtering time. (a) Magnetron sputtering for 1 min, (b) sputtering for 5 min, (c) sputtering for 25 min.

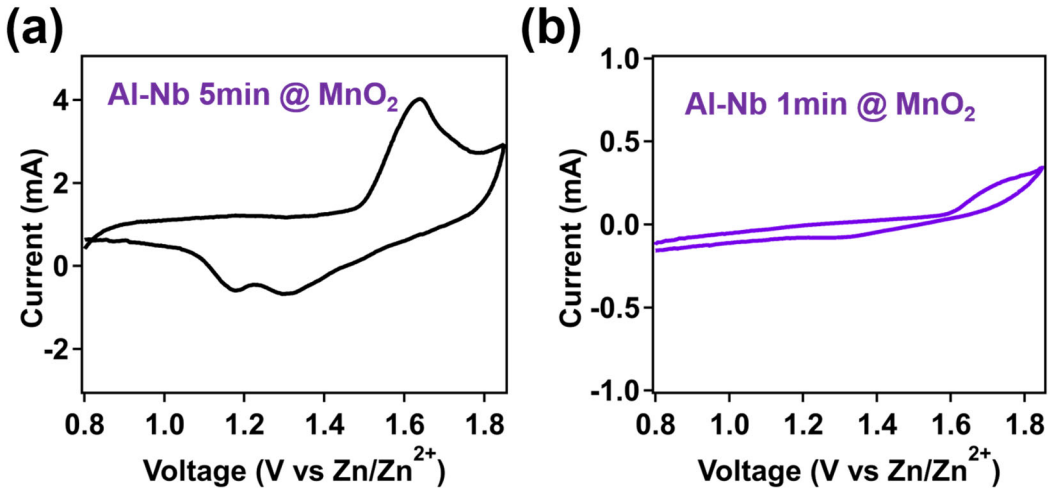

Figure S23. CV curves obtained from (a) the Al-Nb samples prepared by sputtering for 5 min and (b) the Al-Nb samples prepared by sputtering for 1 min. The sweep rate is 0.5 mV s^{-1}.

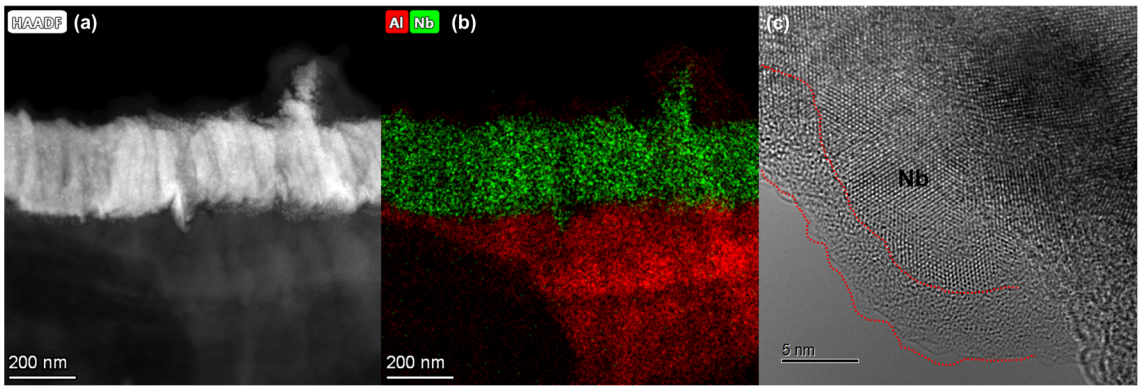

Figure S24. (a) STEM image and (b) the corresponding EDS mapping of the Al-Nb cathode current collector after one charge/discharge cycle. (c) HRTEM micrograph of the Nb coating after cycling. The amorphous oxides layer on the surface of Al-Nb remains a whole after electrochemical cycling, and the Nb-coating structure is also intact, confirming that Nb coating can effectively protect the current collector from damage.

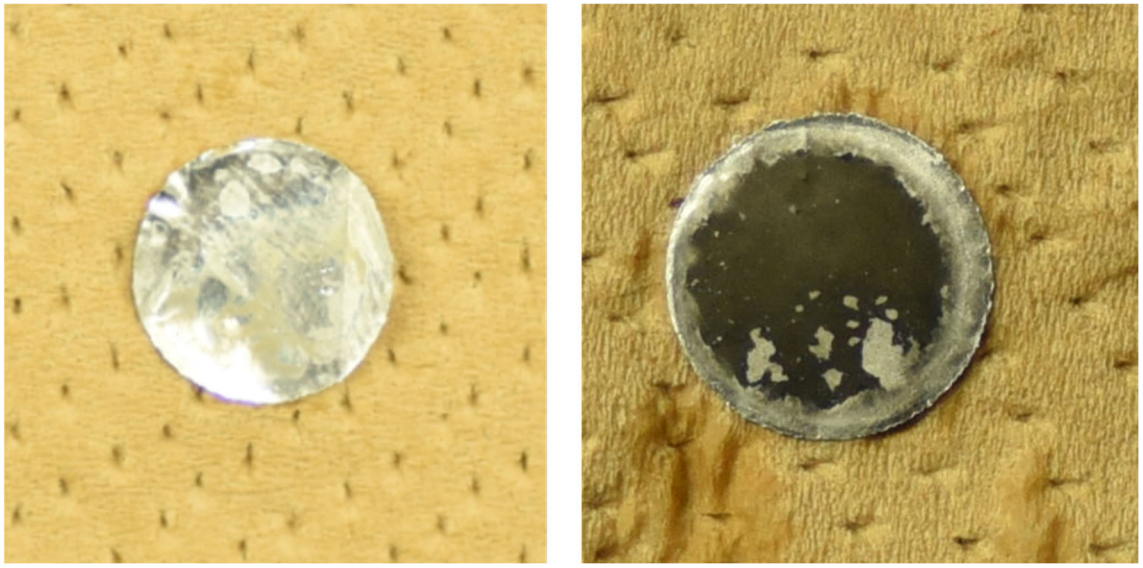

Figure S25. Al-Nb foil (left) and Al foil (right) after immersion in 0.1 M KOH aqueous solution for 24 h.

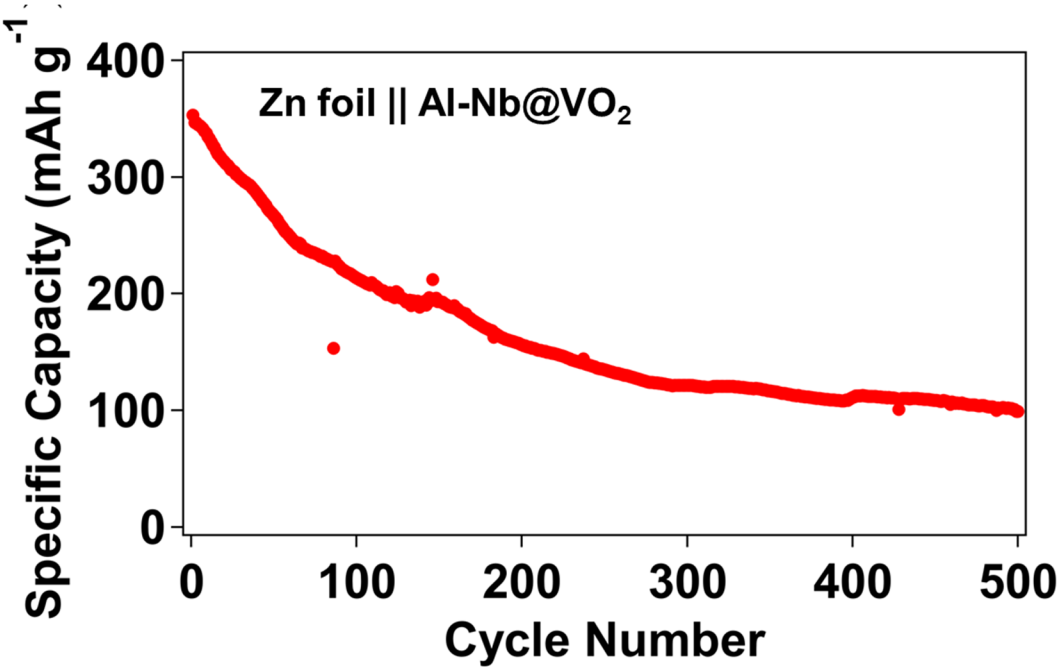

Figure S26. Cycling performance of Zn||VO_2 full cell with the Al-Nb cathode current collector.

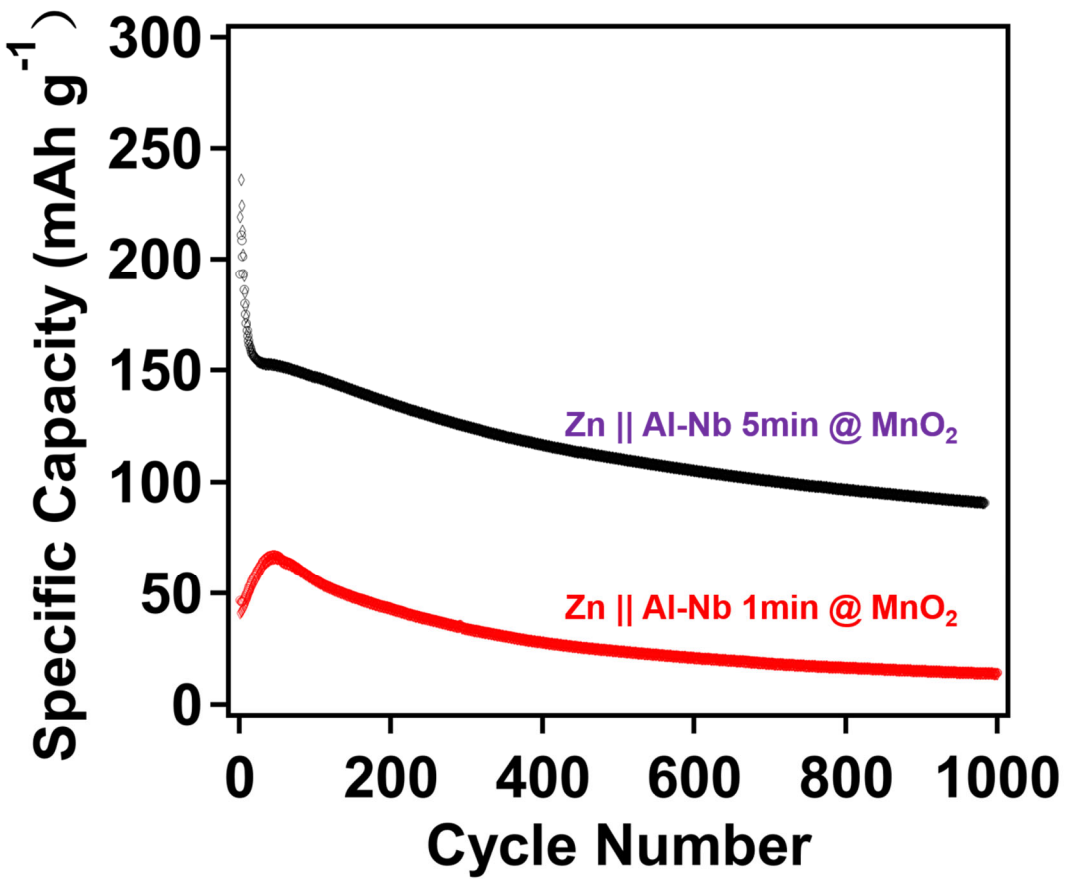

Figure S27. Cycling performance of Zn||MnO_2 full cells with different Al-Nb cathode current collectors.

This result validates our conclusion that magnetron sputtering should take no less than 5 minutes. Carrying out magnetron sputtering for 1 minute is not enough to generate a complete Nb coating on the Al surface.

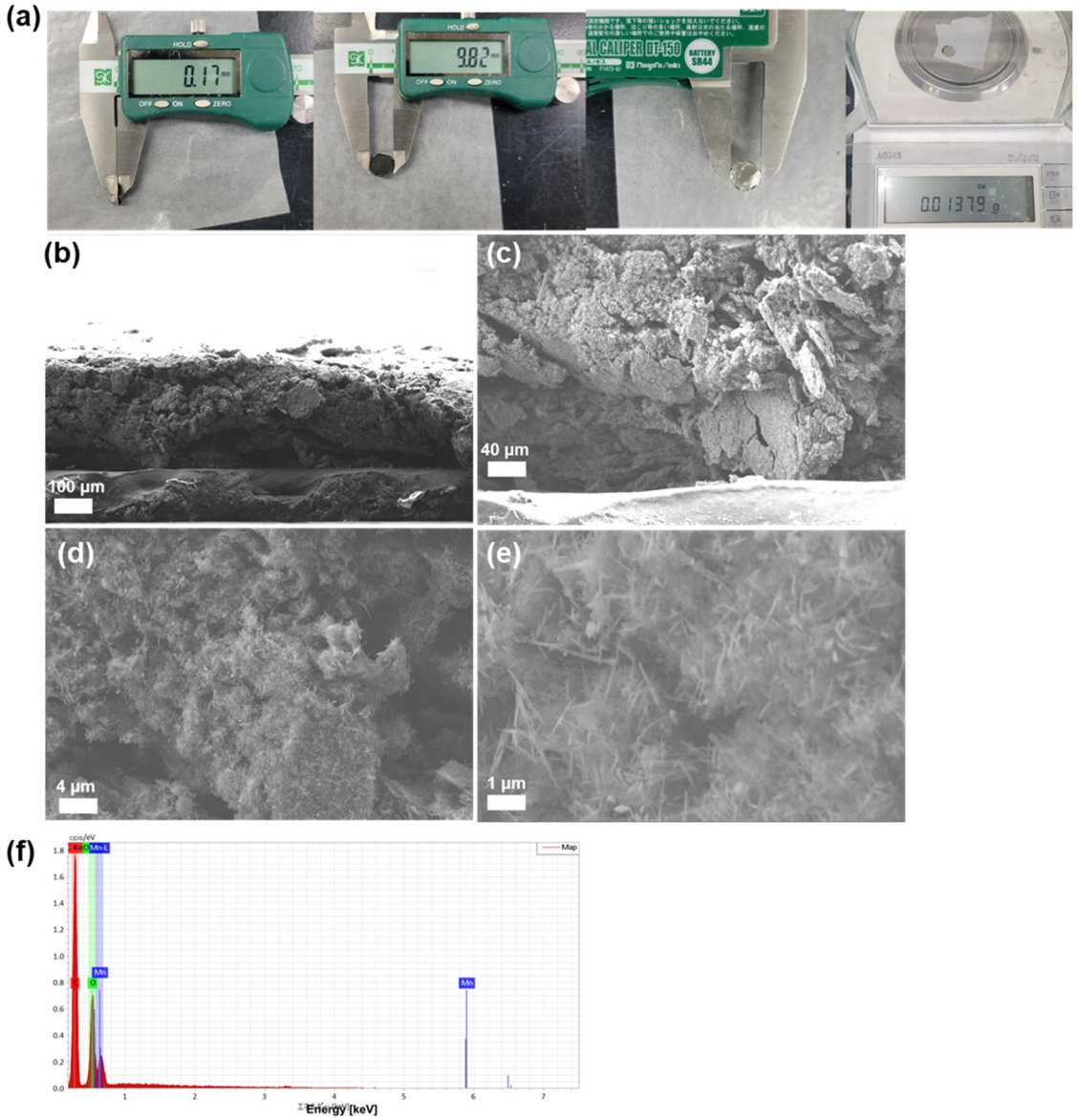

Figure S28. (a) Optical photos of the prepared Al-Nb@MnO_2 electrode and the physical parameters. (b, c, d, e) Cross-sectional SEM images of the Al-Nb@MnO_2 electrode. (f) The elemental mapping of **Figure S28 (e)**. The observed needle-like nanowire is α-MnO_2.

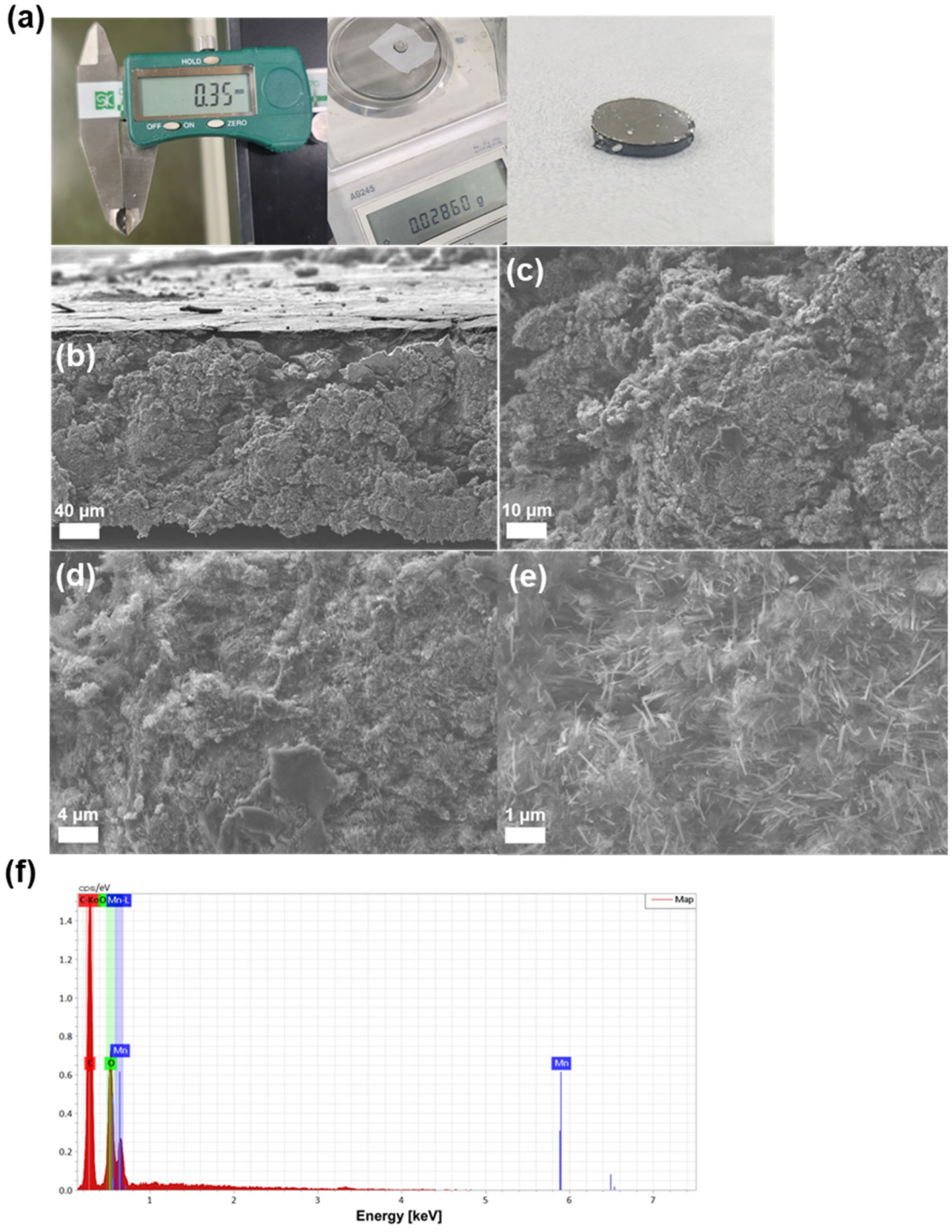

Figure S29. (a) Optical photos of the prepared thick Al-Nb@MnO_2 electrode and the physical parameters. (b, c, d, e) Cross-sectional SEM images of the Al-Nb@MnO_2 electrode. (f) The elemental mapping of Figure S29 (e).

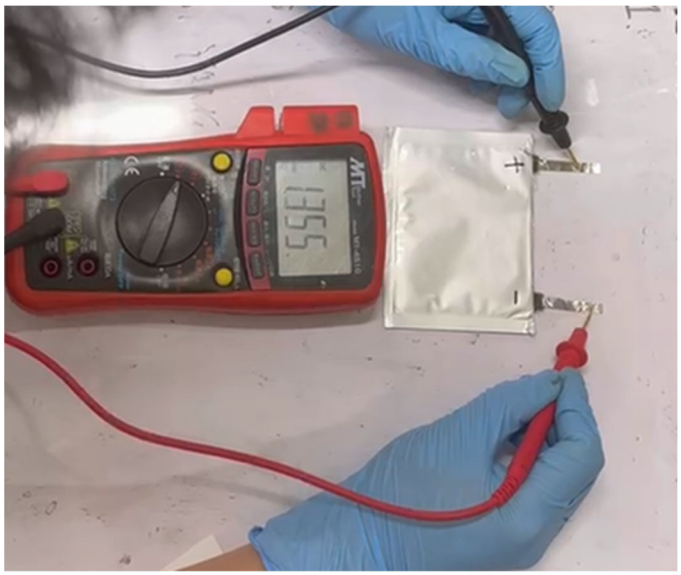

Figure S30. OCV of the pouch cell.

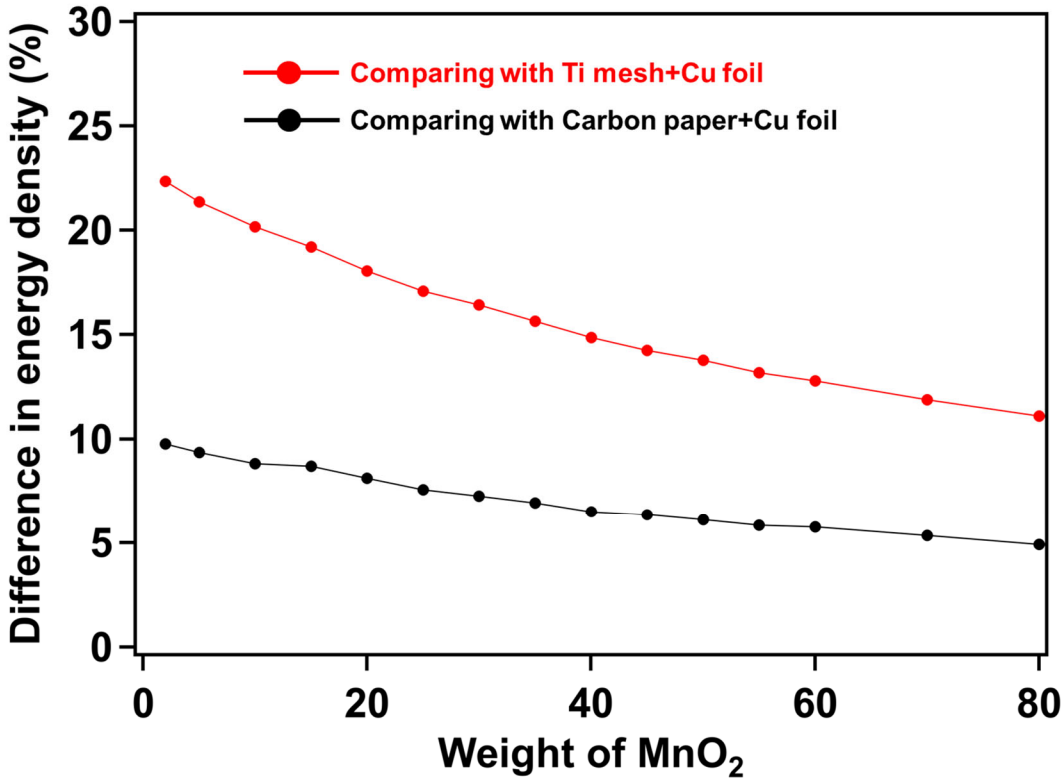

Figure S31. Differences in energy density when different current collectors are used in Zn||MnO_2 pouch cells (based on the parameters shown in Table S1, Table S2 and Table

S3).

The red line in the figure indicates the difference in energy density between the Zn||MnO_2 pouch cells using Al-Nb foil as the anode and cathode current collectors when compared with the cells that use Ti mesh and Cu foil as the anode and cathode current collectors. Similarly, the black line represents the value when it is compared with the cell using carbon paper and Cu foil as the current collectors.

It is apparently that when the cathode loading is within the real-world application range (> 52 mg cm^{-2}, corresponds to a single-layer pouch cell whose energy density is no less than 70 Wh kg^{-1}), the cell using Al-Nb foil as the current collector has a 5% advance in energy density when compared with the cell using carbon paper and Cu foil. It is also notable that the data is calculated based on the one-layer pouch cell, as the number of layers increases, the advantage of using Al-Nb foil will be more obvious.

Table S1. Electrochemical parameters of the pouch cell.

Electrochemical Parameter	Cell
MnO_2 ratio (vs. cathode)	80%
Energy density (5^{th} cycle)	339.8 Wh kg^{-1}
Active area	35 cm^2

Physical Parameter	Cell

Weight composite anode (Zn+Al-Nb)	1.013 g
Weight of cathode	1.31 g
Weight of Al-Nb	0.181 g
Weight of electrolyte	3.17 g
Weight of separator	0.41 g
Package+Tabs	1.48 g

Table S2. Physical parameters of the pouch cell.

Table S3. Physical parameters of different substrates

	Weight (mg)	Area (cm^2)	Thickness (mm)	Areal mass-density (mg cm^{-2})
Al foil	4.05	0.785	0.1	5.16
Al-Nb	4.06	0.785	0.1	5.17
Cu foil	13.72	0.785	0.02	17.48
Ti mesh	22.15	0.785	0.1	28.22
Carbon paper	6.07	0.785	0.04	7.73

Reference

[1] H. Luo, B. Wang, C. Wang, F. Wu, F. Jin, B. Cong, Y. Ning, Y. Zhou, D. Wang, H. Liu, *Energy Storage Mater*. 2020, 33, 390.

[2] R. Zhu, B. H. Yang, W. Cui, L. Fadillah, T. Huang, Z. Xiong, C. Tang, D. Kowalski, S. Kitano, C. Zhu, D. R. King, T. Kurokawa, Y. Aoki, H. Habazaki, *J. Mater. Chem. A.*, 2022, 10, 3122.

[3] G. Kresse, J. Furthmüller, *Comput. Mater. Sci*. 1996, 6, 15−50.

[4] G. Kresse, J. Furthmüller, *Phys. Rev. B* 1996, 54, 11169−11186.

[5] J. P. Perdew, K. Burke, M. Ernzerhof, *Phys. Rev. Lett.* 1996, 77, 3865−3868.

[6] G. Kresse, D. Joubert, *Phys. Rev. B* 1999, 59, 1758-1775.

[7] P. E. Blöchl, *Phys. Rev. B* 1994, 50, 17953−17979.